Brownian motion of soft particles near a fluctuating lipid bilayer

Cite as: J. Chem. Phys. 159, 244903 (2023); doi: 10.1063/5.0182499 Submitted: 19 October 2023 • Accepted: 12 November 2023 • Published Online: 27 December 2023







S. Sheikh, B. Lonetti, 2,3,a) I. Touche, D. A. Mohammadi, Z. Li,4,b) and M. Abbas, 3,c)



AFFILIATIONS

- ¹ Laboratoire de Génie Chimique, Université de Toulouse, CNRS, INPT, UPS, Toulouse, France
- ²IMRCP, UMR5623 CNRS, Université de Toulouse, Toulouse, France
- ³ FR FERMAT, Université de Toulouse, CNRS, INPT, INSA, UPS, Toulouse, France
- Department of Mechanical Engineering, Clemson University, Clemson, South Carolina 29634, USA
- a) Electronic mail: barbara.lonetti@univ-tlse3.fr
- b)Electronic mail: zli7@clemson.edu
- c) Author to whom correspondence should be addressed: micheline.abbas@ensiacet.fr

ABSTRACT

The dynamics of a soft particle suspended in a viscous fluid can be changed by the presence of an elastic boundary. Understanding the mechanisms and dynamics of soft-soft surface interactions can provide valuable insights into many important research fields, including biomedical engineering, soft robotics development, and materials science. This work investigates the anomalous transport properties of a soft nanoparticle near a visco-elastic interface, where the particle consists of a polymer assembly in the form of a micelle and the interface is represented by a lipid bilayer membrane. Mesoscopic simulations using a dissipative particle dynamics model are performed to examine the impact of micelle's proximity to the membrane on its Brownian motion. Two different sizes are considered, which correspond to ≈10 – 20 nm in physical units. The wavelengths typically seen by the largest micelle fall within the range of wavenumbers where the Helfrich model captures fairly well the bilayer mechanical properties. Several independent simulations allowed us to compute the micelle trajectories during an observation time smaller than the diffusive time scale (whose order of magnitude is similar to the membrane relaxation time of the largest wavelengths), this time scale being hardly accessible by experiments. From the probability density function of the micelle normal position with respect to the membrane, it is observed that the position remains close to the starting position during $\approx 0.05\tau_d$ (where τ_d corresponds to the diffusion time), which allowed us to compare the negative excess of mean-square displacement (MSD) to existing theories. In that time range, the MSD exhibits different behaviors along parallel and perpendicular directions. When the micelle is sufficiently close to the bilayer (its initial distance from the bilayer equals approximately twice its gyration radius), the micelle motion becomes quickly subdiffusive in the normal direction. Moreover, the temporal evolution of the micelle MSD excess in the perpendicular direction follows that of a nanoparticle near an elastic membrane. However, in the parallel direction, the MSD excess is rather similar to that of a nanoparticle near a liquid interface.

Published under an exclusive license by AIP Publishing. https://doi.org/10.1063/5.0182499

I. INTRODUCTION

Understanding soft interactions is important for engineering new devices that should interact with biological systems, such as in the biomedical and soft robotics fields. More particularly in biology, endocytosis is one of the most important processes, where species uptake by a living cell occurs through its plasma membrane,¹ erned by complex biophysical and biochemical mechanisms.³ There is a tremendous research effort on the development of drug carriers to vehicle medicines to targeted cells, where the carrier, a hard (gold or silica) or a soft colloid (i.e., liposomes and polymer micelles), should successfully approach the cell membrane and cross it. There is a proof of the efficiency of some of these soft drug carriers at the clinical level, with a limited current understanding of the rules for designing them. An exhaustive description of the soft(drug carrier)-soft(cell boundary) interactions should include the study of the dynamics along the interaction pathway. To simplify the problem, we study in this work a passive interaction of mechanical origin, where electrical and chemical contributions are negligible.

The motion of small particles is controlled by thermal agitation in the absence of interactions. Most of the investigations in the literature addressing Brownian motion of particles near an interface considered rigid colloidal particles. It is well known that confinement by neighboring interfaces alters particle thermal diffusion in a fluid through the modification of particle mobility close to the interface. Near a rigid wall, particle diffusion is decreased compared to its thermal diffusion in an unbounded fluid due to the decrease in particle mobility in both parallel and perpendicular directions (with respect to the wall). This phenomenon was evidenced theoretically⁵ and then experimentally near a plane wall^{6,7} and a cylindrical wall.8 However, if the interface is fluid-like, the diffusive behavior depends on the viscosity of phases on both sides of the interface (see a recent review by Villa et al.9). In case the viscosity of the solvent where the particle is immersed is higher than the viscosity of the fluid on the other side of the interface, the particle mobility in the direction parallel to the interface increases with respect to the unbounded counterpart, unlike the mobility in the perpendicular direction, which is decreased. 10-12 When the interface is membranelike, its bending resistance induces elastic energy storage that leads the Brownian motion to depend on the history of the particle trajectory. 13 It has been shown that this memory effect induces a change in the diffusion motion in time and that the diffusion coefficient is close to its value in the bulk at a short time while it decreases to tend toward the diffusion coefficient near a hard wall at a long time scale, going through a sub-diffusive regime at an intermediate time range.¹⁴ Experiments carried out with diffusive particles (of micron size) near GUV and cell membranes indicate a strong dependence of particle mobility on the nature of the cell (macrophage, adenocarcinoma cell, or epithelial), which is assumed to be associated with the cell's composition and its regulation of proteins and lipids inside the cell or the membrane.15

In the above-mentioned literature, the size of the colloidal particles investigated experimentally is of the order of a micron, which corresponds to a spatial range accessible to optical measurements (confocal microscopy, optical tweezers, and optical interference). The present study investigates the Brownian motion of a soft particle near a soft interface at much smaller length scales inaccessible to optical measurements; the particle size is few tens of nanometers, as typically found in drug delivery applications. The boundary is modeled as a lipid bilayer, representing a model biological membrane. The soft nanoparticle (called micelle hereafter) is designed from the self-assembly of amphiphilic molecules with sizes ~10-20 nm for its potential to carry non-soluble drugs before being easily disintegrated or eliminated by the organism after drug delivery is completed. We use a numerical method accounting for molecular interactions, including hydrophobic and hydrophilic forces, to investigate the system dynamics at constant thermal energy.

The remainder of this paper is organized as follows: in Sec. II, we first briefly introduce the numerical method and describe the details of the micelle-bilayer system setup. Sections III and IV characterize the mechanical properties of the lipid bilayer and the diffusive motion of the micelle. Section V discusses the results of the Brownian motion of the soft micelle near the fluctuating bilayer membrane. Section VI provides conclusions.

II. NUMERICAL MODEL

A. Mesoscopic simulations with DPD

Dissipative particle dynamics (DPD) is a coarse-grained molecular dynamics (MD) simulation technique that is widely used to

study mesoscopic complex fluid phenomena, which are otherwise very difficult to study by the conventional all-atom MD method. $^{16.17}$ Similar to the MD systems, a DPD model is based on the dynamics of interacting particles, which are represented by coarse-grained beads that interact via a set of pairwise forces, whose coarse graining nature allows simulations of fluid systems on a longer time scale and a larger length scale beyond the capability of MD. The time evolution of a DPD bead i with a unit mass of $m_i \equiv 1$ is governed by the Newton's equation of motion, 18

$$\frac{d\mathbf{r}_i}{dt} = \mathbf{v}_i, \qquad \frac{d\mathbf{v}_i}{dt} = \mathbf{F}_i, \tag{1}$$

where the total force \mathbf{F}_i on a DPD bead i comes from three non-bonded pairwise interactions with its neighboring bead j within a cutoff distance beyond which these interactions vanish. The pairwise interactions between DPD particles include a conservative force (\mathbf{F}_{ij}^D) , a dissipative force (\mathbf{F}_{ij}^D) , and a random force (\mathbf{F}_{ij}^D) ,

$$\mathbf{F}_{i} = \sum_{j \neq i} \left(\mathbf{F}_{ij}^{C} + \mathbf{F}_{ij}^{D} + \mathbf{F}_{ij}^{R} \right), \tag{2}$$

$$\mathbf{F}_{ij}^{C} = a_{ij}(1 - r_{ij}/r_c)\hat{\mathbf{r}}_{ij}, \tag{3}$$

$$\mathbf{F}_{ij}^{D} = -\gamma_{ij}\omega_{D}(r_{ij})(\hat{\mathbf{r}}_{ij} \cdot \mathbf{v}_{ij})\hat{\mathbf{r}}_{ij}, \tag{4}$$

$$\mathbf{F}_{ii}^{R} = \delta_{ii}\omega_{R}(r_{ii})dt^{-1/2}\theta_{ii}\hat{\mathbf{r}}_{ii}, \tag{5}$$

where a_{ij} is the conservative force coefficient called the repulsion parameter, $r_{ij} = |\mathbf{r}_{ij}| = |\mathbf{r}_i - \mathbf{r}_j|$ is the distance between particles i and j, and r_c is the cutoff distance for pairwise interactions. $\hat{\mathbf{r}}_{ij} = \mathbf{r}_{ij}/r_{ij}$ is the unit vector pointing from particle j to particle i, and $\mathbf{v}_{ij} = \mathbf{v}_i - \mathbf{v}_j$ quantifies their velocity difference. dt is the time step for time integration of the equation of motion, and θ_{ij} is the Gaussian random variable with a zero mean and unit variance. In addition, γ_{ij} is the dissipative coefficient, and δ_{ij} sets the strength of the random force.

The conservative force is responsible for the static properties of the DPD fluid, which determine the liquid compressibility and solubility. Thus, the value of the repulsion parameter a_{xx} for the same type of particles can be determined by matching the compressibility of the modeling fluid, while the mutual solubilities between different beads are determined by the values of a_{xy} for different types of particles. In general, the Flory–Huggins χ -parameter is linear with respect to the excess repulsion Δa , which is defined by $\Delta a = a_{xy} - a_{xx}$, where a_{xx} represents the same type of beads and a_{xy} stands for different types of beads. Setting repulsion parameters small for same type beads and large for unlike beads will generate a positive Flory–Huggins χ -parameter, leading to phase separation. 19

To have correct canonical distribution functions, the dissipative and random forces are related by satisfying the fluctuation dissipation theorem in the form of Ref. 20,

$$\delta_{ij}^2 = 2\gamma_{ij}k_BT$$
, $\omega_D(r_{ij}) = \omega_R^2(r_{ij}) = (1 - r_{ij}/r_d)^s$, (6)

where k_B is the Boltzmann constant and T is the temperature. ω_D and ω_R are weight functions for dissipative and random forces, respectively. The exponent s changes the shape of the weight functions and is modified to adjust fluid viscosity and diffusion in order to have a reasonable value of the Schmidt number. These two

non-conservative forces together act as a thermostat to maintain an isothermal condition for the DPD fluid. This thermostat is achieved through pairwise interactions and conserves both linear and angular momentum, which leads to the correct description of hydrodynamics. The cutoff radius r_d of the dissipative and random forces is, in general, equal to that of the conservative force r_c in the DPD model. However, r_d can be set to larger values in order to increase the bead momentum transfer with respect to their diffusion.

For bonded DPD particles, i.e., polymers with a chain-like structure, additional bond interactions should be included as well. For example, a harmonic spring quadratic potential is computed by

$$U_{\rm b} = (1/2)k_{\rm b}(r - r_0)^2,$$
 (7)

$$U_{\theta} = (1/2)k_{\theta}(\theta - \theta_0)^2, \tag{8}$$

where r_0 and θ_0 are the equilibrium lengths and angles and k_b and k_θ are the spring constant and angular bending stiffness, respectively.

B. Simulated systems

The system setup consists of lipids self-assembled in a bilayer and amphiphilic surfactant-like molecules self-assembled in micelles freely moving in the solvent, as illustrated in Fig. 1 (the solvent is not shown here for more clarity). Self-assembly is promoted by the initial molecule configuration. The coarse-graining follows closely that pioneered by Groot and Rabone²⁴ and is used frequently in the literature (see Ref. 25 for example). Each DPD bead represents a volume of 90\AA^3 . Since the volume of a water molecule is approximately 30\AA^3 , every DPD bead represents three water molecules. The number density in the simulations is set to $\rho = 3$. Consequently, the characteristic interaction distance between two DPD beads r_c corresponds to the physical length-scale $\sqrt[3]{3} \times 90\text{\AA}^3 = 0.646$ nm. In addition, for the amphiphilic surfactant-like molecules, we

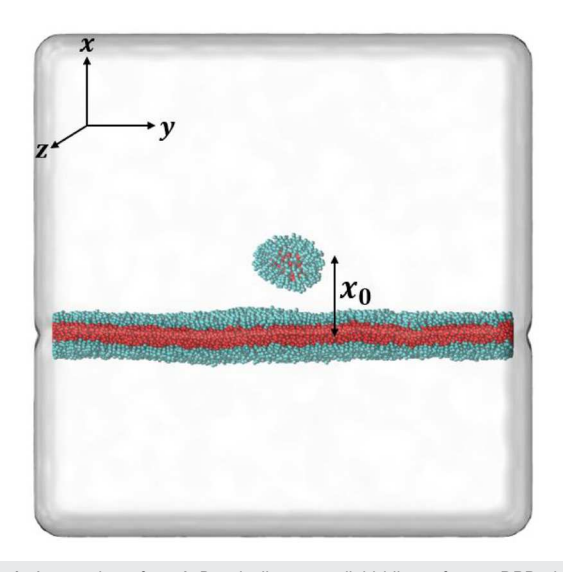


FIG. 1. A snapshot of an A_4B_4 micelle near a lipid bilayer from a DPD simulation. The solvent is transparent. Hydrophobic beads are represented in red, and hydrophilic beads are represented in cyan.

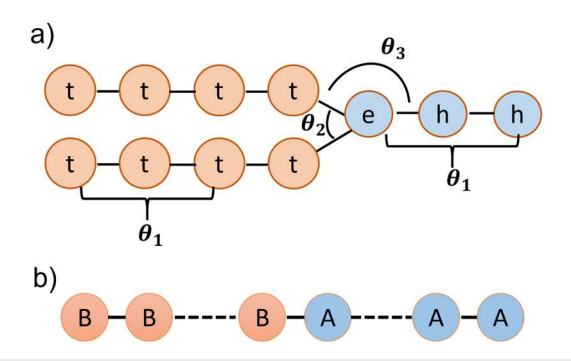


FIG. 2. Coarse-graining of (a) lipid molecules and (b) A_nB_n monomeric molecules.

adopted the same coarse-graining rule, with each DPD bead representing a volume of $90\mathring{A}^3$, which presumes that the density of the whole system is close to that of water.

1. Lipid bilayers

The lipid bilayer was constructed from the assembly of the molecules, such as the one displayed in Fig. 2. It is composed of a polar head segment divided into three hydrophilic beads and two tails formed by four hydrophobic beads each, connected by the glycerol group (the bead e in Fig. 2). Three CH₂ atoms are grouped together to form a hydrophobic t DPD bead. The closest lipid molecules to the one considered here are the DLPC (dilauroyl-sn-glycero-3-phosphocholine, with 12 carbon atoms) and the DMPC (dimyristoyl-phosphatidylcholine, with 14 carbon atoms per tail), the latter being more frequently studied in the literature on lipid bilayers. The interaction coefficients a_{ij} between hydrophobic t, hydrophilic h, and water beads w, as well as the thermal energy $k_B T$, are chosen such that the lipid bilayer falls into the fluid phase, according to the study of Kranenberg and Smit. ²⁶ Those coefficients are summarized in Table I.

2. Micellar system

The micelle is made of amphiphilic chains with equal hydrophobic and hydrophilic segments. The smallest micelle considered for this work is similar to a micelle formed of a nonionic surfactant $C_{12}E_6$. The corresponding coarse-graining leads to a chain of four hydrophobic and four hydrophilic DPD beads. This molecule will be called A_nB_n hereafter, where each B bead represents an $(CH_2)_3$ group and each A bead represents 1.5 ethylene oxide (EO) groups (see Groot and Rabone²⁴ for more details). With respect to

TABLE I. DPD beads are classified into three types: solvent beads (w), hydrophilic beads (h, e, or A), and hydrophobic beads (t or B). In this work, the conservative interaction rules for beads e, h, and A are identical, and the conservative interactions for beads t and B are also identical.

a	W	h	t
w	25	15	80
h	15	25 80	80 80 25
t	80	80	25

the interaction coefficients a_{ij} , the beads A and B are, respectively, equivalent to h and t. This analogy reflects situations where the solubility of the lipid chains is close to that of the surfactant-like molecule in the solvent.

C. Simulation setup

The software LAMMPS is used to carry out simulations at constant volume, number of beads, and thermal energy. The simulation box is periodic in all directions. L_x , L_y , and L_z denote the box dimensions in the x, y, and z directions, respectively. These dimensions will be marked explicitly for the different simulations carried out. The water molecules fill the simulation box after the bilayer and/or micelle molecule positions and orientations are initialized. The two leaflets of the bilayer contain an equal number of lipid molecules. These molecules are initially disposed parallel to the yz plane in a way to promote their self-assembly in the form of a bilayer. The micelle is formed with an aggregation number set to 200 for any micelle size; the self-assembly is initially promoted by orienting the hydrophobic segments of the chains toward the micelle center at the beginning of the simulation. The micelle remains stable, with no fragmentation events observed in the frame of the simulations carried out for this work.

The simulation results are expressed in terms of length (r_c) , time $(r_c\sqrt{m_0/k_BT})$, and energy (k_BT) in DPD units. The correspondence between the simulation time unit and the physical time will be given once the characteristic time scales are discussed in Sec. V. The simulations carried out for this study cost around two million central processing unit (CPU) hours (the most time consuming simulations being those carried out for Sec. V).

D. Simulation parameters

In the simulations, we set the thermal energy to $k_BT=0.8$ and the exponent in the weight function of the dissipative force to s=0.5, following Li *et al.*'s work.²⁷ A uniform random number generator has been used for this work, as it takes less CPU time than the Gaussian random number generator, while no statistical difference was found between these two types of generators.²⁴ As for the bond springs, we set the linear stiffness to $k_b=100$, the equilibrium distance between connected beads to $r_0=0.7$, and the bending stiffness to $k_\theta=6.0$. The equilibrium angles between two adjacent bonds are $\theta_{10}=180^\circ$, $\theta_{20}=90^\circ$, and $\theta_{30}=135^\circ$, as illustrated in Fig. 2.

For the other parameters, two considered sets are summarized in Table II. In the first one, called SET1 hereafter, standard DPD $\,$

TABLE II. SET1 and SET2 parameters, expressed in DPD units: thermal energy k_BT , exponent s used in Eq. (7), cutoff of the conservative force r_c , cutoff of the random and dissipative forces r_d , time step dt, amplitude of the random force δ , dynamic viscosity η , and Schmidt number Sc (the viscosities and diffusion coefficients are obtained from Li et al.'s work²⁷). The thermal energy is $k_BT = 0.8$, and the exponent of the weighting function is s = 0.5.

	r_c	r_d	dt	δ	η	Sc
SET1	1.0	1.0	0.01	3	1.7	7.5
SET2	1.0	1.3	0.005	5	16.2	443

parameters are used. The cutoff radius $r_c=1$ is identical for the conservative, dissipative, and random pairwise forces. The strength of the random force is $\delta=3$, and accordingly, $\gamma=\delta^2/2k_BT=5.625$. The time step is dt=0.01. In another set of simulations called SET2, the cutoff distance of the conservative force is maintained equal to 1. However, the cutoff distance for the dissipative and random forces is set to $1.3r_c$. The strength of the random force is $\delta=5$, and correspondingly, $\gamma=15.625$. The time step dt=0.005 guarantees the simulation stability.

Those parameters allowed for adjusting the diffusion coefficient and viscosity of the DPD model (a similar strategy has been used, for instance, by Pieczywek et al.²⁸): the dynamic viscosity is larger and the DPD bead diffusion is smaller in simulations based on SET2 compared to the SET1. The ratio between the kinematic viscosity and diffusion of the DPD beads leads to the characteristic dimensionless Schmidt number Sc. The values of Sc corresponding to SET1 and SET2 parameters are included in Table II. Those values are calculated theoretically following the work of Li et al.,27 assuming a uniform pair bead distribution. One can also calculate, directly from the numerical simulations, the fluid viscosity (obtained from the Poiseuille flow profile of a DPD fluid submitted to constant body force) and self-diffusion coefficient (obtained from the mean square displacement of the DPD beads submitted to k_BT). In that case, the numerical values obtained with SET1 are $\eta = 1.86$ and D = 0.11, leading to Sc = 5.6, whereas the numerical values obtained with SET2 are $\eta = 17.1$ and D = 0.01, leading to Sc = 570. The discrepancies between the numerical and theoretical values of η and D are of the order of 10%. The Schmidt numbers suggest that in SET1 simulations, the DPD fluid exhibits rather gas-like dynamics, whereas in SET2 simulations, the DPD fluid exhibits liquid-like dynamics.

III. BILAYER PROPERTIES

Lipid membranes belong to a special class of membranes that can be easily deformed by external stress and also experience thermal fluctuations that increase their configurational entropy. Depending on the conditions (temperature, pressure, and hydration), a lipid bilayer can go through a variety of phases. The phase of the bilayer is also influenced by structural characteristics, such as head group size and hydrophobic tail length. The parameters used in this study, particularly the interaction coefficients and the thermal energy, lead the lipid bilayer to behave as a fluid phase.²⁶

The simulations are carried out with squared membranes in order to promote the spatial symmetry of the membrane fluctuations. The box dimensions in the y and z directions are $L_y = L_z = L$. As the simulation box is periodic in the y and z directions, the value of L sets the area per lipid molecule a, such that $N_la/2 = L^2$, with N_l denoting the total number of lipid molecules in the bilayer $(N_l/2)$ is the number of lipid molecules in one leaflet). In order to verify the bilayer state, we calculated the bilayer thickness and its order parameter S. The bilayer thickness t_b can be defined in different ways. In our study, it is calculated from the average distance between the top hydrophilic heads in the two leaflets. The bilayer thickness is found to be $t_b = 6.50[r_c]$ in simulations based on both SET1 and SET2. The order parameter is given by

$$S = \frac{\left(3\cos^2(\alpha) - 1\right)}{2},\tag{9}$$

TABLE III. Summary of the bilayer mechanical properties obtained from numerical simulations

	$K_A \left[k_B T / r_c^2 \right]$	$\kappa [k_BT] [\text{Eq.} (12)]$	κ [k_BT] [Eq. (14)]
SET1	23.1	16.2	24.4
SET2	23.6	16.6	22.7

where α denotes the angle between the vector connecting the first and last beads in the tail of a lipid molecule and the bilayer normal. The brackets denote the ensemble average over the lipid molecules. Asymptotically, the order parameter tends to 1 if the average lipid tails are parallel to the normal to the bilayer surface, to -0.5 if they are perpendicular, and to 0 if the tail orientation is random. In most of the simulations carried out for this work, the order parameter is found to be around 0.3, indicating that the bilayer behaves as a fluid.

A. Static properties

Next, the bilayer mechanical properties are calculated, particularly the surface tension, the area compressibility (or dilatation modulus), and the bending rigidity. The results are summarized in Table III. In atomistic simulations, the surface tension can be calculated from the averaged difference between normal stress p_{xx} and tangential stresses $(p_{yy} + p_{zz})/2$ (with respect to the normal to the interface),²⁹

$$\sigma = \frac{1}{L^2} \int_{V} \left[p_{xx} - \frac{1}{2} (p_{yy} + p_{zz}) \right] dV, \tag{10}$$

where L^2 represents the membrane projected surface and V denotes the volume of the simulation domain. In general, when the membrane is not stretched and not subject to external potentials, it adopts a tensionless state. In the absence of external potential, the membrane surface tension depends on the area per lipid molecule a. The simulations are realized with two bilayer sizes: a smaller one with $N_l = 3200$ and a larger one with $N_l = 12\,800$. The corresponding box size is $(L_x, L, L) = (24.2, \sqrt{N_l a/2}, \sqrt{N_l a/2}) r_c^3$. Then, several simulations are carried out with different areas per lipid molecule a. The resulting time average surface tension is calculated in a steady state. The results are displayed in Fig. 3.

Several key points in the interface mechanics can be highlighted in Fig. 3. First, at a small area per lipid, the surface tension becomes negative due to membrane buckling, as in the simulations in Ref. 31. In that case, the surface tension depends on the membrane's finite size. This feature is inherent to numerical simulations of lipid bilayers with periodic boundaries. Beyond the area per molecule that leads to the tensionless state, when the membrane is stretched, the surface tension increases due to the excess in free energy as hydrophobic chains are relatively more exposed to the solvent. The increase in the area per molecule is linear (which leads to membrane apparent elasticity) up to a certain limit where the membrane reaches plastic yielding until it breaks at large areas (beyond the limit shown in Fig. 3). In the linear regime, the slope allows us to calculate the area compressibility K_A defined in the frame of the Helfrich model for membranes as

$$\sigma = K_A \frac{\left(a - a_0\right)}{a_0},\tag{11}$$

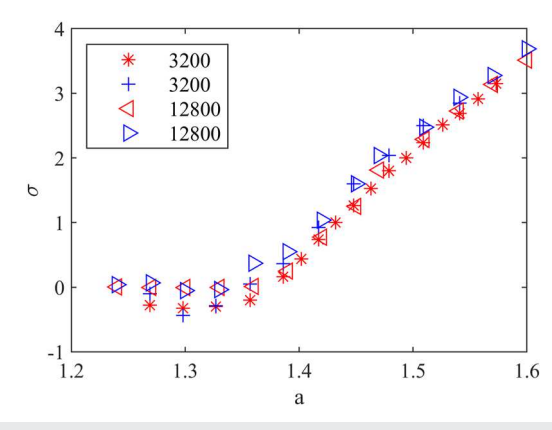


FIG. 3. Bilayer surface tension as a function of the area per lipid for two different sets of parameters, SET1 (red color) and SET2 (blue color). The curves are obtained with two bilayer sizes, the smallest containing 3200 lipids and the largest containing 12 800 lipids. The surface tension is in DPD units (k_BT/r_c^2) .

where a_0 corresponds to the area per lipid that leads to vanishing surface tension. In Fig. 3, a_0 is estimated to be around $1.38[r_c^2]$, which would correspond to 57.6\AA^2 , which is close to what can be found from measurements on phosphocholine lipids in fluid state, between 56 and 70\AA^2 , depending on the hydrophobic chain length. 33,34

Figure 3 also suggests that the surface tension and the area compressibility are almost independent of the DPD parameters used in both SET1 and SET2 (except in the buckling region, which is not the case of interest for this study) and that the domain size has no significant influence on the slope in the plots. Therefore, K_A , calculated from the slope of the surface tension curve in the linear regime, is not significantly dependent on the simulation parameters: $K_A = 23.1[k_BT/r_c^2]$ and $23.6[k_BT/r_c^2]$ for SET1 and SET2, respectively, with the results being very close for both bilayer sizes. Those values of the area compressibility are close to available experimental measurements for DMPC bilayers ($K_A = 23.8[k_BT/r_c^2]$ in the work of Rawicz *et al.*,³⁵ which corresponds to 0.234 N/m) and to available numerical simulations ($K_A = 21.66[k_BT/r_c^2]$ in the work of Gao *et al.*³⁶ and $K_A = 23[k_BT/r_c^2]$ in the work of Li *et al.*²⁹).

One of the most significant mechanical characteristics of the lipid bilayer is its bending rigidity. The amount of energy needed to change the membrane's normal curvature into a different out-of-plane curvature is known as the bending modulus of the lipid bilayer and will be called κ .

In the frame of the elastic theory, a lipid bilayer is assumed to behave as an elastic sheet, where the bending rigidity is related to the area compressibility as follows:³⁰

$$\kappa = K_A \frac{t_b^2}{48},\tag{12}$$

where t_b is the bilayer thickness. Based on the calculated values of K_A and t_b , Eq. (12) leads to $\kappa = 16.2[k_BT]$ ($\approx 6.6 \times 10^{-20}$ J at room temperature) for SET1 and $16.6[k_BT]$ ($\approx 6.8 \times 10^{-20}$ J) for SET2.

Another way of calculating the bending rigidity κ in particle-based models starts with the Helfrich Hamiltonian. For membranes

that deviate only weakly from the plane, the position of the midplane (the plane between both leaflets) can be described by the Monge parameterization h(r); the Helfrich Hamiltonian is then $H=0.5\int_S \left[\kappa(\nabla^2h)^2+\sigma(\nabla h)^2+U\right]dS+const.^{37-39}$ The contribution of external potentials denoted by U will be neglected in the following ways: When h(r) is expanded in a Fourier series, assuming that the Fourier modes h_q decouple, applying the Fourier transform of the Helfrich Hamiltonian and the equipartition theorem, the equilibrium power spectrum of the height fluctuations can be written as

$$\langle |h_q|^2 \rangle = \frac{k_B T}{L^2 (\kappa q^4 + \sigma q^2)}.$$
 (13)

The bracket $\langle \cdot \rangle$ represents time averaging in each simulation. When the bilayer is tensionless, i.e., σ is negligible, the bending rigidity can be calculated from the relation

$$\langle |h_q|^2 \rangle = \frac{k_B T}{L^2 (\kappa q^4)}. \tag{14}$$

The simulations used to calculate $\langle |h_q|^2 \rangle$ contain $N_l = 12\,800$ lipid molecules, and the box size is $(L_x, L_y, L_z) \approx (93[r_c])^3$. The calculated interfacial tension (in DPD units) is $\sigma = 0.02[k_BT/r_c^2]$ for SET1 and $0.05[k_BT/r_c^2]$ for SET2, respectively. At the post-processing level, a two-dimensional linear mesh with 32×32 grid points is defined over the area of the bilayer. In every snapshot, the bilayer height is calculated at each grid point h(y,z) by the average normal coordinate of the surrounding hydrophobic beads. Next on that grid, the height fluctuations are calculated with respect to the average bilayer height as well as the corresponding Fourier transform.

The power spectrum of the height fluctuations is displayed in Fig. 4. Note that periodic boundary conditions lead to a maximum wavelength equal to L. In the limit of small wavenumbers (high wavelengths), $\langle |h_q|^2 \rangle$ scales like q^{-4} and κ can be obtained from a simple fit, whereas the description of the lipid bilayer by the Helfrich

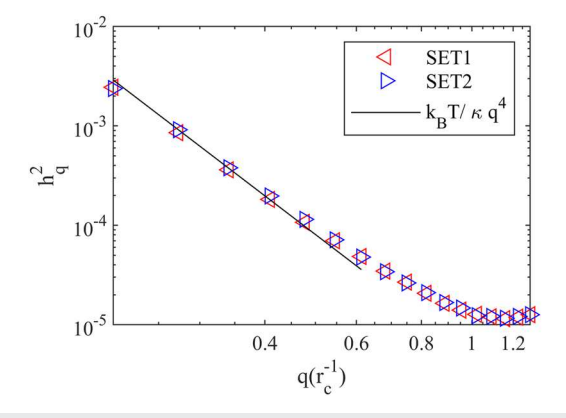


FIG. 4. Fluctuation spectrum (h_q^2) of the tensionless bilayer as a function of wavenumber (q). The line represents the theoretical fit [using Eq. (14)], the red triangles represent the calculated spectrum from the SET1 simulations, and the blue triangles represent the SET2 simulations.

model breaks at high wavenumbers. In Eq. (14), the bending rigidity κ is calculated in the limit of small wavenumbers, provided that the membrane surface tension is small: $\kappa \approx 24.4k_BT$ and $22.7k_BT$ for SET1 and SET2 simulations, respectively.

To end this section, we compare our results on bending rigidity with values from the literature, which are numerous and suffer from scattering in some situations. It should be noted that experimental results usually depend on the measurement technique, and numerical results can depend on the size of the studied membranes, as reported in the review by Bochicchio and Monticelli. 40 For DMPC bilayers at room temperature, κ was found to be in the range $29-34[k_BT]$ using shape fluctuations optical analysis in the experiments of Nagle et al., 41 whereas $\kappa = 6.9 \times 10^{-20}$ J (which corresponds to $16.8[k_BT]$), ³⁵ using the micropipette pressurization technique. Other experiments based on x-ray scattering carried out by Tristram-Nagle et al.⁴² on DLPC bilayers led to $\kappa = 5.5 \times 10^{-20}$ J (which corresponds to $13.4[k_BT]$) at room temperature. As for the bending rigidity from numerical simulations (based either on surface undulation or on the membrane buckling technique), one can find $\kappa \approx 24-36[k_BT]$ at room temperature obtained from atomistic⁴³ or coarse-grained simulations.⁴⁴ The values of κ measured from numerical simulations tend to increase with the box size and the measurement time, while κ measured from thermal undulation analysis depends on whether lipid tilt is taken into account or not when calculating κ .⁴⁰ The values of bending rigidity found from area compressibility are smaller than those mentioned above. In numerical simulations of DMPC bilayers, Gao et al.³⁶ found $\kappa = 8[k_BT]$ (with $K_A = 21.7[k_BT/r_c^2]$), whereas Li et al.²⁹ found $\kappa = 11[k_BT]$ (with $K_A = 23[k_BT/r_c^2]$). These values are smaller than the ones found in the present work for two possible reasons: the bending rigidity calculated from the undulation method [Eq. (14)] increases with the box size (for instance, the membrane surface in Gao et al.'s work³⁶ is 33 times smaller than that in the present work), and the bending rigidity calculated from the compressibility method [Eq. (12)] is strongly influenced by the way the thickness is evaluated.³⁰

B. Dynamic properties

The rate of undulation relaxation is the main dynamic property that we have investigated. Since this quantity requires the measurement of the friction coefficient of the two monolayers sliding one past the other, we will first start by calculating this quantity. For this purpose, simulations (with SET1 parameters) were realized with $N_l = 3200$ and a box size equal to $(L_x, L, L) = 46.6^3 r_c^3$. The fluid in the box undergoes shear flow, with the average vorticity being parallel to the membrane plane. The shear was imposed by moving two slabs at x = 0 and $x = L_x$ at equal and opposite velocities V_{yw} in the y direction. Figure 5(a) shows a typical velocity profile at a steady state, obtained by averaging the velocity beads in slabs parallel to the membrane. One can clearly observe the discontinuity in the slope of the velocity profile dV_{ν}/dx between the solvent region, where the shear rate deviates slightly from the one that the solvent would experience in the absence of the bilayer, and the smaller slope in the bilayer, which corresponds to a much stronger resistance to shear deformation. We define v_s , the slip velocity between the solvent and the bilayer, from the intersection between the two linear approximations of the velocity profiles in both flow regions, as indicated

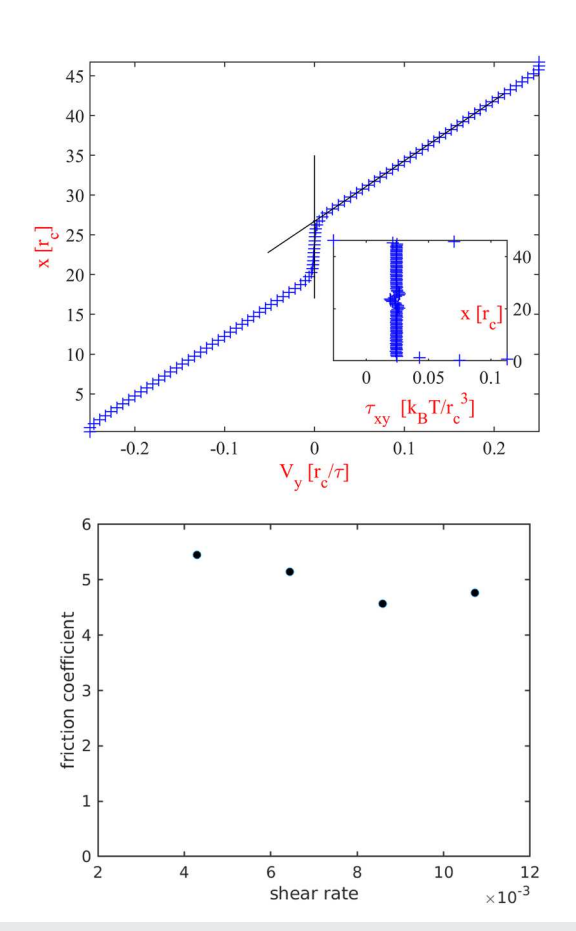


FIG. 5. Bilayer under shear flow. (a) Velocity profile $V_y(x)$ from DPD simulations displayed in blue plus symbols. The lines are obtained from linear approximations of the velocity profile in the bulk and the bilayer. The inset shows the shear stress along the x direction. (b) Friction coefficient $b\left[\sqrt{mk_BT}/r_c^3\right]$ of the two monolayers sliding one past the other as a function of the imposed shear flow $2V_{wy}/L_x[r_c/\tau]$.

in Fig. 5(a). The friction coefficient follows from the shear stress τ_{xy} exerted by the solvent on the top and bottom monolayers, using

$$b = \frac{\tau_{xy}}{\nu_s}. (15)$$

The shear stress τ_{xy} has been computed by averaging the shear stress experienced by the DPD beads in slabs parallel to the membrane (the domain has been divided into ≈ 100 slabs along x). As one expects in the frame of momentum conservation along the flow direction in the Couette flow, the shear stress is constant along x in the solvent phase; it slightly fluctuates across the bilayer around the average value. Within the fictitious walls, the measured stress is insignificant, and the values were thus excluded from the average. The friction coefficient calculated with Eq. (15) is displayed in Fig. 5(b) as a function of the shear rate. The average value of the friction coefficient is $b \approx 5[\sqrt{mk_BT}/r_c^3]$, which would correspond to $\approx 4 \times 10^5$ Ns/m³ at room temperature. This value, like others obtained in the past by molecular simulations of lipid bilayers, 45,46 is typically smaller by two orders of magnitude compared to experimental values for DMPC bilayers. 47,48 This difference is attributed to

the fact that coarse-graining leads to the speed-up of the dynamics in general, in addition to the fact that the small size of the membrane in numerical simulations reduces the macroscopic apparent roughness induced by large scale undulations.

Next, the dynamics of bilayer thermal undulations was studied by considering the undulation mode autocorrelation. Seifert and Langer⁴⁹ have shown that b manifests itself through the decay of the autocorrelation function of the undulatory modes. They have solved the overdamped equations of motion of a bilayer coupled with those of the solvent. The bilayer consists of two layers of bending rigidity κ and elastic modulus k_m , surrounded by the solvent of viscosity η . Coupled sets of equations of motion for the height and projected density difference (between the two lipid layers) were written by Seifert and Langer, considering that modes with different wave-vectors evolve independently. The slowest relaxation rates that emerge from their analysis depend on the mode wavenumber, compared to a critical wavenumber, $q_c = (2\eta k_m)/(b\tilde{\kappa}) \approx 0.073[r_c^{-1}]$ Following Shkulipa et al.,⁵⁰ for $q > q_c$, the slowest relaxation rate is $\gamma_{rs1} \approx \frac{k_m \kappa}{2h} q^2$ occurs from the two layers slipping one on top of the other, whereas for $q < q_c$, the slowest relaxation rate is $\gamma_{rb1} \approx \frac{\kappa}{4n} q^3$ falls into the bending regime. The Onsager regression hypothesis is usually invoked to describe the autocorrelations of height around equilibrium, $C(q,t) = \langle h_q(t)h_q^*(0)\rangle/|h_q^2| \approx e^{-\gamma_{r1}t}$, considering only the dominant decay.

We attempted to validate the decay in time of the undulation autocorrelation function. For this, we carried out numerical simulations where the bilayer normal displacement field h(y, z, t) was saved frequently in time. SET1 parameters were used for this test. As for the calculation of the bending rigidity, h(y, z, t) was constructed on a (32×32) grid, with the normal displacement averaged over the x positions of the beads in the lipid tails that belong to a grid element. Since the relaxation time of the different modes increases significantly with the wavenumber, we carried out a simulation during $60\,000\tau$ and time sampling equal to τ to analyze modes (1,0) $(q = 0.068r_c^{-1})$ and (1,1) $(q = 0.095r_c^{-1})$, and a last simulation during 1500 τ and time sampling every 0.02 τ to analyze modes (2,0), (2,1), and (3,0) (q = 0.135, 0.151, and 0.203 r_c^{-1} , respectively). The undulation autocorrelation function for the different modes is displayed in Fig. 6, together with $C(q,t) = e^{-\gamma_{rs1}t}$. The autocorrelation function for the three largest wavenumbers follows an exponential decay $\sim q^2 t$, unlike the smallest wavenumbers. In a short time, the height fluctuations of the smallest wavenumbers decay exponentially like $\sim q^3 t$, as expected by the theory. The coefficient in front of $q^3 t$ that leads to the best estimate (see Fig. 6) is equal to $1/5 \times \kappa/(4\eta)$ instead of $\kappa/(4\eta)$. The fact that the relaxation time is slower than what is expected from the theory of Siefert and Langer is probably associated with the bilayer inertia in the simulations.⁵

IV. MICELLE SIZE AND SELF-DIFFUSION

Simulations with three particle (or micelle) sizes were carried out, considering different chain lengths for A_4B_4 , A_6B_6 , and A_9B_9 molecules, respectively, using both SET1 and SET2 parameters. The micelle radius of gyration R_g informs us about the micelle compactness associated with hydrophobic and hydrophilic atom distribution. Experimentally, it can be inferred from small-angle neutron scattering (SANS) and small-angle x-ray scattering (SAXS)

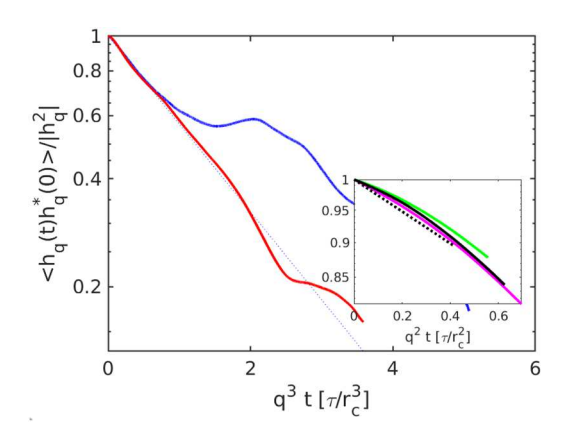


FIG. 6. Normalized undulation autocorrelation functions in time, for different wavenumbers. The blue, red, green, magenta, and black colors correspond to $q=0.068,\,0.095,\,0.135,\,0.151,\,{\rm and}\,0.203r_c^{-1},\,{\rm respectively}.$ The light dotted line in the main panel corresponds to $e^{-\frac{1}{5}\gamma_{tot}t}$. The dotted line in the inset corresponds to $e^{-\gamma_{st}t}$.

measurements. In numerical simulations, the instantaneous radius of gyration is calculated using

$$R_{g} = \frac{1}{N} \sqrt{\sum_{i=1}^{N} |\mathbf{x}_{i} - \mathbf{x}_{c}|^{2}},$$
 (16)

where \mathbf{x}_c denotes the center of mass and \mathbf{x}_i refers to the position of a hydrophobic or hydrophilic bead i in the polymer molecules. The time average value is included in Tables IV and V. The micelle has another important dimension to be considered: the hydrodynamic radius (R_h) associated with the micelle diffusive motion. The hydrodynamic radius (also called Stokes radius in the literature) of an object corresponds to the radius of a hard sphere that diffuses at the same rate as that object. The relation between R_h and the micelle diffusion coefficient can be written in terms of the Stokes–Einstein relation,

$$D_0 = \frac{k_B T}{6\pi n R_b},\tag{17}$$

where D_0 refers to the isotropic diffusion coefficient in the bulk and η corresponds to the solvent dynamic viscosity. Experimentally, the diffusion coefficient and, subsequently, the hydrodynamic radius are often measured using dynamic light scattering (DLS). Similarly, in the present simulations, the diffusion coefficient D_0 is

TABLE IV. Simulation results using SET1 parameters: micelle radius of gyration $R_g[r_c]$, diffusion coefficient $D[r_c^2/\tau_{DPD}]$, hydrodynamic radius $R_h[r_c]$, and the ratio between the box length and the micelle size $L/2R_g$.

	R_g	D_0	R_h	$\frac{R_g}{R_h}$	$\frac{L}{2R_g}$
A_4B_4	4.50	0.0029	8.72	0.44	8.89
A_6B_6	5.30	0.0021	12.03	0.48	8.96
A_9B_9	6.40	0.0015	16.85	0.38	7.42

TABLE V. Idem Table IV for simulations using SET2 parameters.

	R_g	D_0	R_h	$\frac{R_g}{R_h}$	$\frac{L}{2R_g}$
$\overline{A_4B_4}$	4.44	0.000 34	7.72	0.63	9.00
A_6B_6	5.30	0.00027	9.73	0.50	8.96
A_9B_9	6.42	0.000 18	14.59	0.51	7.40

calculated from the slope of the mean square displacement (MSD) of the micelle motion at "long times" using

$$D_0 = \frac{1}{2} \lim_{t \to \infty} \frac{d(MSD)}{dt},\tag{18}$$

where we consider the MSD of the center-of-mass of the micelle, which is defined as $\mathbf{X} = \sum m_i \mathbf{x}_i / \sum m_i$. MSD is computed from the Einstein formula $\mathrm{MSD}(\tau) = \langle |x(t+\tau) - x(t)|^2 \rangle = N^{-1} \sum_{i=1}^N |x(t_i+\tau) - x(t_i)|^2$, with N being the number of samples. To maximize N for a stable measure of MSD, we use a sliding time window⁵² with a duration time to average over all possible lag-times $\tau < \tau_{\mathrm{max}}$, where τ_{max} is the duration of the trajectory obtained from numerical simulations.

The micelle MSD is computed within a simulation domain sufficiently large in order to minimize the interaction of the micelle with its images through the periodic boundaries. For each micelle, the MSD is averaged over the three spatial directions (isotropic diffusive motion) and over six independent trajectories. The temporal evolution of the corresponding ensemble-averaged MSD is displayed in Figs. 7 and 8 using SET1 and SET2, respectively. At a short time scale (up to 100 DPD time units), the micelle experiences a ballistic motion where the MSD increases as t^2 . Beyond that time, the MSD increases linearly in time, with good signal convergence in the time interval [200-1000] DPD time units, which corresponds approximately to $[0.02-0.1]\tau_{d1}$ in simulations based on SET1 and $[0.003-0.02]\tau_{d2}$ in simulations based on SET2 [where τ_d denotes the micelle diffusion time scale, see Eq. (19)]. The diffusion coefficient is estimated from the linear increase in the MSD in this time range using Eq. (18).

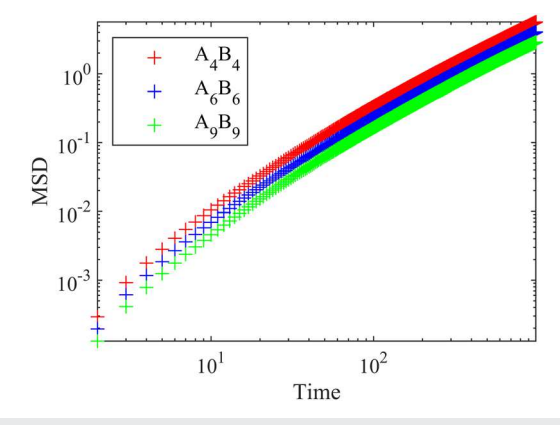
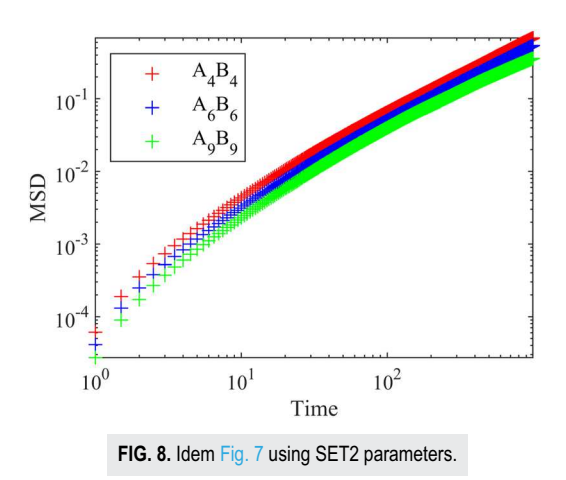


FIG. 7. Evolution of MSD $[r_c^2]$ in time $[\tau_{DPD}]$ for different micelle sizes from simulations using SET1 parameters.



The diffusion coefficients are included in Tables IV and V for different micelle radii and simulation parameters. Those tables also contain the hydrodynamic radius, calculated from Eq. (17), which is not a geometric quantity but corresponds to the radius of the sphere that experiences similar self-diffusion under thermal agitation. The results show that the ratio between the gyration radius and hydrodynamic radius of the micelle is smaller than 0.75, corresponding to a filled sphere, and closer to that of a core-shell object.⁵³ It is interesting, although, to compare the hydrodynamic radius to the radius of the fictitious sphere that would be obtained if the polymer chains were concentric and straight with the bond at equilibrium. In that case, the chain length would have been equal to the number of elements multiplied by the bonds equilibrium length (set to $0.7r_c$ in the present simulations). The radius of that object would be equal to $5.6r_c$, $8.4r_c$ and $12.6r_c$ for A_4B_4 , A_6B_6 , and A_9B_9 , respectively, falling between the gyration and hydrodynamic radius. This indicates that the micelle has a larger response time to thermal agitation, even when compared to a full sphere of radius equal to the fictitious "spiky" sphere. It is not surprising since the mobility of an object decreases with its permeability with respect to the solvent, as if a slip exists between the object surface and the ambient fluid (discontinuity in the momentum transfer at the object interface). Note that R_h is systematically larger in SET1 simulations compared to SET2, suggesting that the apparent slip is stronger in a gas-like medium than in a liquid-like medium.

V. MICELLE BROWNIAN MOTION NEAR THE LIPID BILAYER

A. Time scales at play

The time a micelle takes to diffuse over a surface equal to its size squared can be estimated based on the Stokes–Einstein relation,

$$\tau_d = \frac{6\pi\eta R_h^3}{k_B T},\tag{19}$$

where R_h refers to the hydrodynamic radius of the micelle. Close to a soft membrane, the particle motion is subject to memory effects associated with membrane undulations and solvent mediated hydrodynamic interactions. The modification of the mean-square displacement of a hard nanoparticle in the presence of

an elastic membrane has been studied theoretically by Bickel, ¹³ where the bilayer bending rigidity was accounted for, and later by Daddi–Moussa–Ider *et al.* (DMI), ⁵⁴ where membrane elasticity (stretching and shear) was also considered. In Sec. V D, we will summarize the results of the DMI theory and compare the time evolution of the MSD obtained numerically with the theoretical one in Sec. V C. Two additional time scales, associated with the membrane properties and the solvent viscosity, emerge. For over-damped membrane surface waves and accounting for velocity continuity and stress jump, two time scales appear in the mobility of a particle located at a distance x_0 near the membrane, one associated with bending,

$$T_b = \frac{4\eta x_0^3}{\kappa},\tag{20}$$

and another time scale associated with the membrane resistance to shear and area dilatation, which can be written as

$$T_s = \frac{6\eta x_0}{K_s},\tag{21}$$

where K_s is the dynamic elastic shear modulus, as written in the theoretical work of DMI.⁵⁴ Unlike red blood cells, in lipid bilayers, the static elastic shear modulus is negligible. However, the dynamic shear modulus can be different from zero at high frequencies, especially when complex interactions take place, and its order of magnitude is about a hundred times smaller than the elastic dilatation modulus, ^{55,56} i.e., $K_s \approx K_A/100$. Thus, in the frame of our simulations, $T_s \ll T_b$, and therefore, viscoelastic effects on the particle motion in the parallel direction are weaker than in the perpendicular direction. It should be noted that the ratio between the micelle diffusion and membrane relaxation time scales is independent of the fluid viscosity. As the values of the bending rigidity obtained from both SET1 and SET2 simulations are close, the ratio τ_d/T_b is close in both simulations, and it ranges roughly between 1 and 100, with x_0 ranging between five and two times the particle radius of gyration, respectively.

At this point, we can give more information about the DPD time scale and its correspondence with physical time. In the DPD simulations, the time scale associated with the bead thermal motion can be written as $\tau_{DPD} = r_c \sqrt{m/k_b T}$. Based on the coarse-graining system, one DPD time unit is thus equivalent to 2.67×10^{-12} s at room temperature. Consequently, the diffusion coefficient of the A_4B_4 micelle obtained from simulations with SET1 parameters, i.e., $D = 2.9 \times 10^{-3} [r_c^2/\tau_{DPD}]$ corresponds to 4.5×10^{-10} m²/s, whereas the diffusion coefficient from simulations with SET2 parameters, i.e., $D = 3.4 \times 10^{-4} [r_c^2/\tau_{DPD}]$ corresponds to 5.3×10^{-11} m²/s. The latter value agrees with typical diffusion coefficients measured with surfactant micelles (such as $C_{12}E_6$) in aqueous solutions.⁵⁷

Thus, simulations with SET2 parameters allow for the correct capture of micelle diffusion on the one hand and the solvent Schmidt number on the other. We can conclude that, among both sets of parameters, SET2 would be more convenient to capture the system dynamics correctly. Yet, τ_d/T_b is close in both sets of simulations (the viscosity drops out in the ratio), so we expect that the relative influence of the membrane on the micelle diffusion would be fairly well captured by the simulations with SET1 parameters. We chose to carry out the following simulations with SET1 parameters since

TABLE VI. Initial distance of the micelle with respect to the membrane midplane (expressed in terms of the gyration radius of each micelle) X_0^n and X_0^f , and the associated ratio between the time scale of viscous relaxation of membrane fluctuations at the micelle position T_b and the diffusion time scale τ_d .

	$X_0^n[R_g]$	$X_0^f[R_g]$	$T_b _{@X_0^n}/\tau_d$	$T_b _{@X_0^f}/ au_d$
A_4B_4	2.5	5.34	0.01	0.12
A_9B_9	1.87	3.75	0.002	0.016

they are significantly cheaper from a computational point of view. Indeed, the diffusion time scale is about ten times smaller in SET1 than in SET2 simulations, and the time step should be twice smaller with SET2 parameters to enhance computational stability.

B. Trajectories

As discussed above, we examine the Brownian motion of a micelle near a lipid bilayer using simulations of type SET1 and with two sizes, i.e., A_4B_4 and A_9B_9 micelles. The lipid bilayer in the simulations contained 12 800 lipid molecules. The simulations were carried out in a cubic box with $(L_x, L_y, L_z) = (93r_c)^3$. The average surface tension of the lipid bilayer calculated *a posteriori* in each simulation is equal to $0.06[k_BT/r_c^2]$. The corresponding capillary length scale is $l_c = \sqrt{\kappa/\sigma} \approx 20r_c$. In order to examine the impact of its distance to the membrane, the micelle was initially placed at two different positions with respect to the bilayer midplane: X_0^n and X_0^f , which refer to positions more or less close to the membrane surface. Those positions, expressed in terms of the micelle radius of gyration, are included in Table VI.

Figure 9 shows a typical trajectory of the A_9B_9 micelle near the membrane. Note that here and in the following, the position along x is calculated with respect to the membrane midplane. This figure was recorded during $\tau = 0.05\tau_d$, with the micelle center of the mass position being recorded every DPD time unit, which corresponds to $\approx 5 \times 10^{-6}\tau_d$. The trajectory contains a clear signature of Brownian motion. The probability density function (PDF) of the micelle position along the normal direction was then calculated over an ensemble of 16 trajectories. The PDF is displayed in Fig. 10 for both A_4B_4 and A_9B_9 placed at X_0^n , from 16 independent trajectories. This

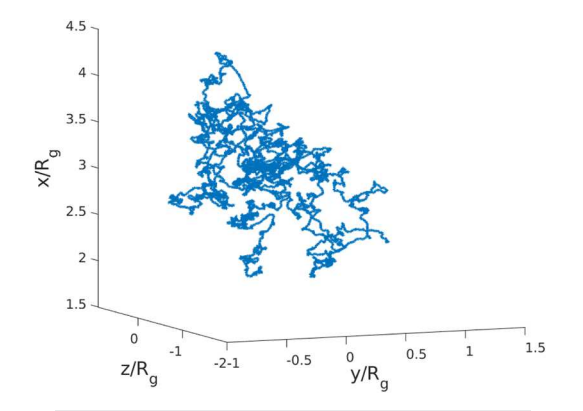
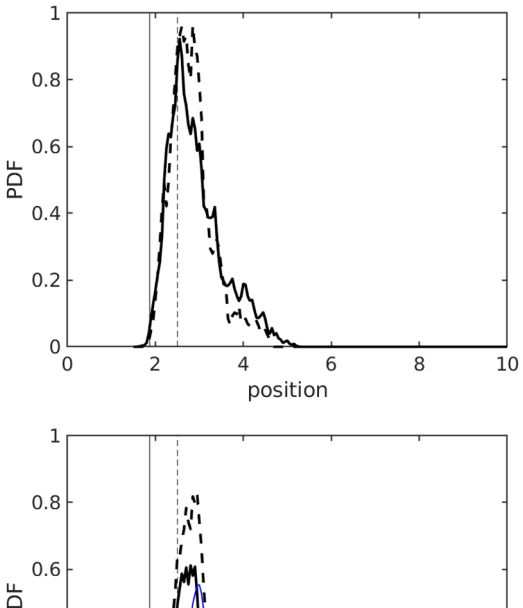


FIG. 9. 3D trajectory of micelle A_9B_9 near a bilayer (at X_0^n).



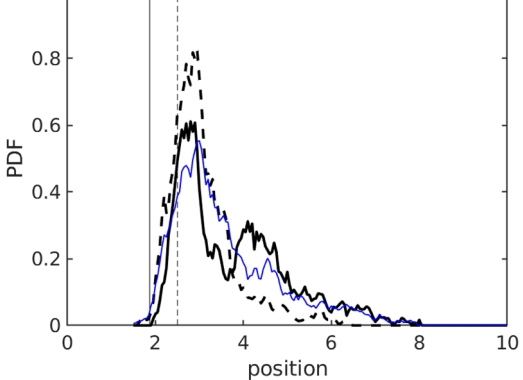


FIG. 10. PDF of the micelle position along x (calculated with respect to the membrane midplane) during (a) $\tau \approx 0.05\tau_d$ and (b) $\tau \approx 0.1\tau_d$ simulation times. The position is scaled by the radius of gyration R_g . The solid and dashed black lines correspond to A_9B_9 and A_4B_4 , respectively, with the vertical solid and dashed lines indicating the corresponding initial position X_0^n . The blue curve in (b) is obtained with A_4B_4 during $\tau \approx 0.3\tau_d$ simulation time.

figure shows that the micelle center of mass deviates slightly from X_0^n but remains close to it during $\tau = 0.05\tau_d$ [panel (a)]. After a time $\tau = 0.1\tau_d$, the PDF remains skewed, peaking near X_0^n , but micelle A_9B_9 spans a wider range of normal positions. Panel (b) shows that A_4B_4 remains close to its initial position for a longer time compared to A_9B_9 . This information will be used during the analysis of the mean-square displacement.

C. Mean-square displacement and scaling exponent

From the micelle center of mass recorded in time, we calculated the MSD separately in parallel and perpendicular directions. Different simulations were carried out starting from two different positions, X_0^n and X_0^f , and for different micelle sizes, A_4B_4 and A_9B_9 . For each initial position and micelle size, the MSD was calculated from an ensemble average over 16 independent simulations. The MSD curves are plotted in Fig. 11 using the logarithmic scale. In this figure, the time is scaled by the diffusion time scale τ_d calculated from Eq. (19), which is independent of the micelle position and the membrane fluctuations. In a short time, an almost quadratic dependence over time can be observed. At longer times, the MSD

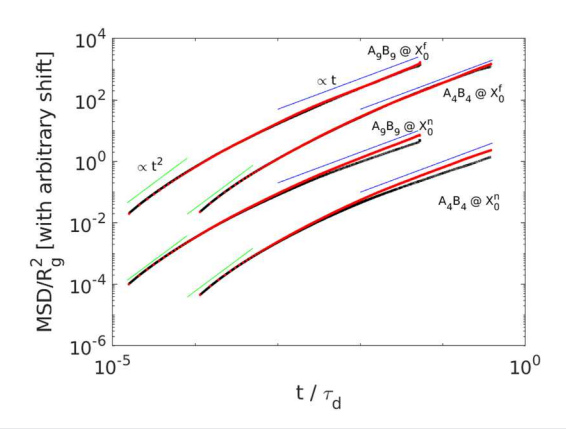


FIG. 11. Evolution of the MSD in time (scaled by τ_d) on a log–log scale for different micelle sizes and initial positions. The red and black lines correspond to the MSD in the parallel and perpendicular directions, respectively. The quadratic and linear trends are shown in light green and blue colors, respectively.

temporal evolution becomes close to linear, especially in the parallel direction, which indicates that the Brownian motion is fairly diffusive in this direction during the measured time range, which allows for estimation of a diffusion coefficient.

For further analysis, it is also insightful to compare the measurement time with characteristic time scales associated with the membrane resistance to deformation. In principle, the relaxation time scale of the largest wavelength $\tau_r = 4\eta L_y^3/\kappa$ is larger than the diffusion time: $\tau_r \approx 8.5\tau_d$ for A_4B_4 and $\tau_r \approx 1.2\tau_d$ for A_9B_9 . Thus, our measurements are carried out during short times compared to τ_r . For this reason, we will scale the time by the bending time T_b from Eq. (20), where the characteristic length is the distance between the particle center and the membrane. The bending-to-diffusive time scale ratio T_b/τ_d corresponding to our simulations is included in Table VI. By construction, T_b is proportional (i) to the third power of the separation distance x_0 and (ii) to the ratio η/κ (such as the relaxation time τ_r). However, it does not take into account the particle's finite size compared to its distance to the membrane.

The scaling exponent $\alpha_i = \frac{dln(MSD_i)}{dlnt}$ calculated both in parallel and perpendicular directions, is displayed in Fig. 12. $\alpha_i \rightarrow 2$ is characteristic of ballistic motion, whereas $\alpha_i \rightarrow 1$ is characteristic of diffusive behavior. Our results indicate two trends in the intermediate time range: in the parallel direction, the scaling exponent tends to level off near 1 for both X_0^n and X_0^f . However, in the normal direction, the scaling exponent clearly decreases below 1 only when the particle is initially placed at X_0^n . Although exact values of this exponent cannot be extracted from our data due to the limited number of available trajectories, the quasi-plateau remains close to 0.9 when the number of trajectories considered to calculate this exponent is varied (40 trajectories were carried out with A_9B_9 for this aim). Moreover, the transition to subdiffusive motion occurs after a time t close to the bending time T_h . This is more clear when the micelle is placed at X_0^n since T_b is much smaller than the simulation time in that case. Note that since we used the sliding time window technique to calculate the MSD and the associated scaling exponent, the statistical convergence becomes weaker over a longer period of time, which leads to large fluctuations of the scaling exponent.

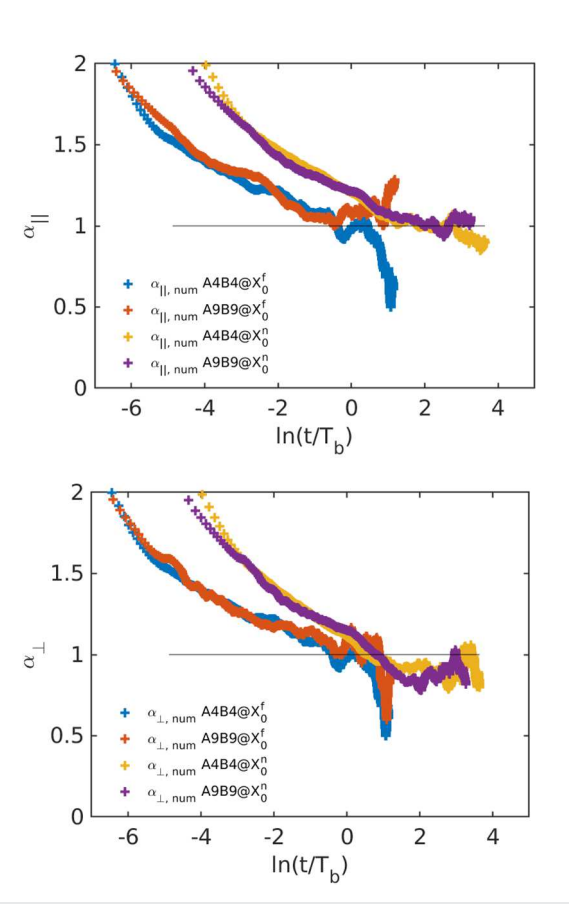


FIG. 12. Scaling exponent of the micelle MSD as a function of time (see the definition in the text) in the parallel direction (a) and the perpendicular direction (b). The time is scaled by the bending time T_b , included in Table VI. The curves are obtained by averaging over 16 trajectories, except $A_9B_9@X_0^n$, which is obtained from 40 trajectories.

Figures 13 and 14 display a lin-lin plot of the temporal evolution of the MSD of A_4B_4 and A_9B_9 micelles, respectively, while scaling the time with τ_d . In each figure, panel (a) displays the MSD very close to the membrane (at X_0^n), whereas panel (b) shows the MSD at a slightly larger distance, (X_0^f) . At first glance, the MSD plots deviate from those of the isolated micelle at X_0^n , reflecting the fact that the micelle has experienced hydrodynamic interactions with the membrane during the observation time scale. However, the MSD plots at X_0^f remain close to those of the micelle in the solvent. This suggests weak hydrodynamic interactions with the membrane, both directly and through the box periodic boundaries (in the normal direction) during the observation time range.

At time $t \ll T_b$, the particle does not "feel" the membrane presence, as first suggested by the analysis of Bickel¹³ considering a Brownian particle near a fluid membrane. However, at $t \gg T_b$, the particle motion becomes independent of the elastic properties of the membrane, as if the particle is moving close to a non-deformable interface. The deviation of the MSD curve at the closer and farther positions can be interpreted in light of the theoretical conclusion of Bickel. In the measurement time range, the significant difference in

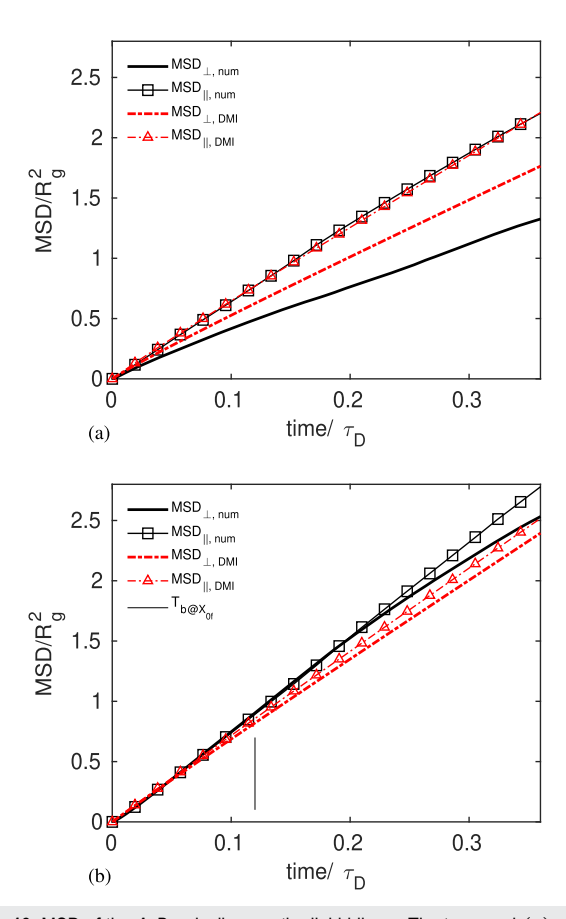


FIG. 13. MSD of the A_4B_4 micelle near the lipid bilayer. The top panel (a) corresponds to particle distance from the membrane equal to X_0^n , whereas the bottom panel (b) corresponds to X_0^f . Lines with (resp. without) symbols correspond to the MSD in the parallel (resp. perpendicular) direction. The black color with sold lines indicates numerical results. The red curves are obtained from Eqs. (22) and (23), using the theory of DMI's work,⁵⁴ with $\kappa = 30 [k_BT]$ being the membrane bending rigidity and $K_A = 18 [k_BT/r_c]$ being the area dilatation taken from the numerical results on the bilayer mechanical properties. Using C = 100, this leads the area strain modulus (which has not been measured directly) to be of the same order as the surface tension $\approx 0.2 [k_BT/r_c^2]$. The vertical line in panel (b) indicates the time of viscous relaxation of membrane fluctuations at the initial particle position. This time tends to zero in panel (a), and thus, it is not shown there.

the dynamics at $x_0 = X_0^n$ and $x_0 = X_0^f$ is due to the time scale required for the particle to feel the membrane presence in addition to the change in particle mobility due to the membrane proximity. T_b estimated at the initial micelle position is indicated by vertical lines in Figs. 13(b) and 14(b) (it is not indicated in panels (a) because T_b/τ_d is very small when $x = X_0^n$). In addition, for the sake of comparison, Figs. 13 and 14 include the curves in red from the theory of DMI (that will be explained further in Sec. V D). One does not necessarily expect perfect matching in view of the differences in system nature, i.e., freely moving soft micelles in the simulations vs trapped solid particles in the theory and elastic membranes vs fluid interfaces. Nevertheless, at the closest separation distance X_0^n , the MSD curves from the DMI theory follow a trend similar to the MSD curves from the numerical simulations. Note that the theoretical MSDs do

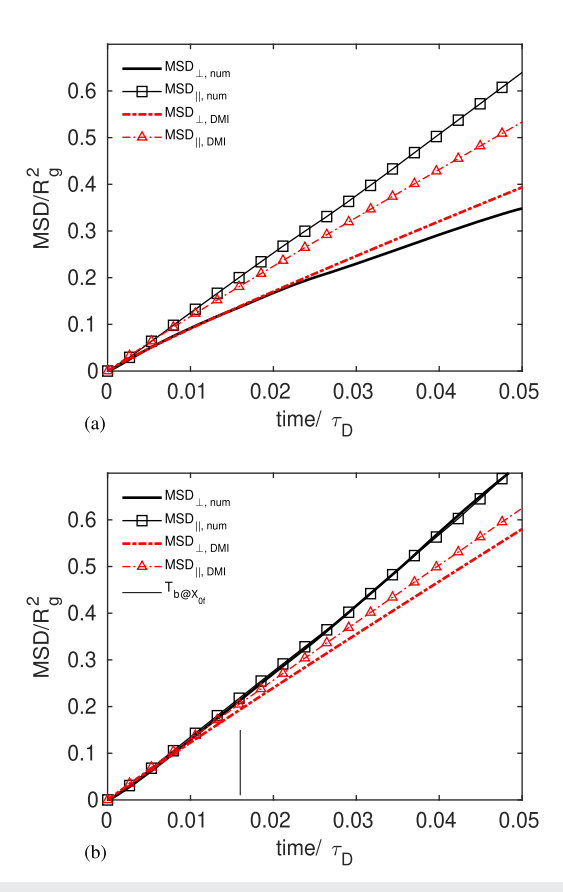


FIG. 14. MSD of the A_9B_9 micelle near the lipid bilayer. The top panel (a) corresponds to particle distance from the membrane equal to X_0^n , whereas the bottom panel (b) corresponds to X_0^f . The data are visualized in the same way as in Fig. 13.

not change significantly when the area compressibility K_A is varied by 10% that is the typical error in the estimation of K_A from the simulations.

D. MSD excess

The MSD negative excess Δ expresses the deviation of the MSD of a Brownian particle with respect to the MSD corresponding to the particle's diffusive motion in the bulk (far from any boundary). In view of the anisotropy of the motion near the membrane, we define the MSD excess separately in the normal and parallel directions with respect to the membrane as follows:

$$\frac{MSD_x}{2D_0t} = 1 - \Delta_{\perp}(t), \tag{22}$$

$$\frac{MSD_{y}}{2D_{0}t} = \frac{MSD_{z}}{2D_{0}t} = 1 - \Delta_{\parallel}(t), \tag{23}$$

where $MSD_x = \langle (x(t) - x_0)^2 \rangle$, $MSD_y = \langle (y(t) - y_0)^2 \rangle$, and $MSD_z = \langle (z(t) - z_0)^2 \rangle$, with brackets referring to an ensemble average.

The MSD excess depends on the relative distance x_0/R and on dimensionless time, where R denotes the particle radius. There are three known limits in the literature for a Brownian particle near an

interface. First, near a hard wall, the MSD excess of a Brownian particle can be written at the leading order in R/x_0 following Happel and Brenner⁵ as

$$\Delta_{\parallel}^{wall} = \frac{9}{16} \frac{R}{x_0}, \quad \Delta_{\perp}^{wall} = \frac{9}{8} \frac{R}{x_0}.$$
 (24)

Second, the MSD negative excess corresponding to a Brownian particle near a liquid interface (referred to with the superscript LL) was derived at the leading order in R/x_0 by Lee $et\ al.$, 10

$$\Delta_{\parallel}^{LL} = \frac{3}{32} \frac{R}{r_0}, \quad \Delta_{\perp}^{LL} = \frac{15}{16} \frac{R}{r_0}.$$
 (25)

The third limit corresponds to the motion of a nanoparticle near a visco-elastic membrane. Assuming an infinitely large membrane that exhibits fluctuations associated with the motion of a nearby nano-particle (the membrane thermal undulations are neglected), negligible inertial effects, and a small change in the particle position compared to its distance x_0 with respect to the membrane, DMI⁵⁴ calculated the negative excess of the particle MSD near the membrane, both in parallel and perpendicular directions. In each direction, this MSD excess is equal to the sum of the strain and bending contributions, written as follows:

$$\Delta_{\perp,s}(\tau) = \frac{3}{16} \frac{R}{x_0} \frac{\tau(3B + 2\tau)}{2(B + \tau)^2}, \qquad (26)$$

$$\Delta_{\perp,b}(\tau_{\perp,b}) = \frac{15}{8\pi} \frac{R}{x_0} \left[\arctan \tau_{\perp,b}^{1/3} - \frac{2}{\tau_{\perp,b}^{1/3}} + \frac{2}{\tau_{\perp,b}} \ln \left(1 + \tau_{\perp,b}^{2/3} \right) \right], \qquad (27)$$

$$\Delta_{\parallel,s}(\tau) = \frac{3}{64} \frac{R}{x_0} \left[\frac{(2\tau + 3B)(5\tau + 4B)}{(B + \tau)^2} - \frac{4B}{\tau} \ln \left(1 + \frac{\tau}{B} \right) - \frac{16}{\tau} \ln \left(1 + \frac{\tau}{2} \right) \right], \qquad (28)$$

$$\Delta_{\parallel,b}(\tau_{\parallel,b}) = \frac{3}{32} \frac{R}{x_0} \left[\frac{\tau_{\parallel,b}^{3/2} + 2\tau_{\parallel,b} + 9\tau_{\parallel,b}^{1/2} + 6}{\tau_{\parallel,b}^{1/2} (1 + \tau_{\parallel,b}^{1/2})^2} - \frac{6}{\tau_{\parallel,b}} \ln \left(1 + \tau_{\parallel,b}^{1/2} \right) \right]. \qquad (29)$$

The constant B=2/(1+C) depends on C, the ratio between the area compressibility and shear modulus of the membrane. There are three dimensionless times that appear in the expressions of the Δ functions, i.e., $\tau=t/T_s$, $\tau_{\parallel,b}=(5/2)(t/T_b)$, and $\tau_{\perp,b}=(9\pi/4)(t/T_b)$. The time scale separation accounts for the difference in the relaxation time associated with membrane bending, resistance to shear, and area dilatation. Bending resistance influences particle diffusion mainly in the perpendicular direction, whereas shear resistance influences the particle displacement rather in parallel direction.

Figure 15 shows the transient evolution of the MSD negative excess [Eqs. (22) and (23)] from simulations carried out with the

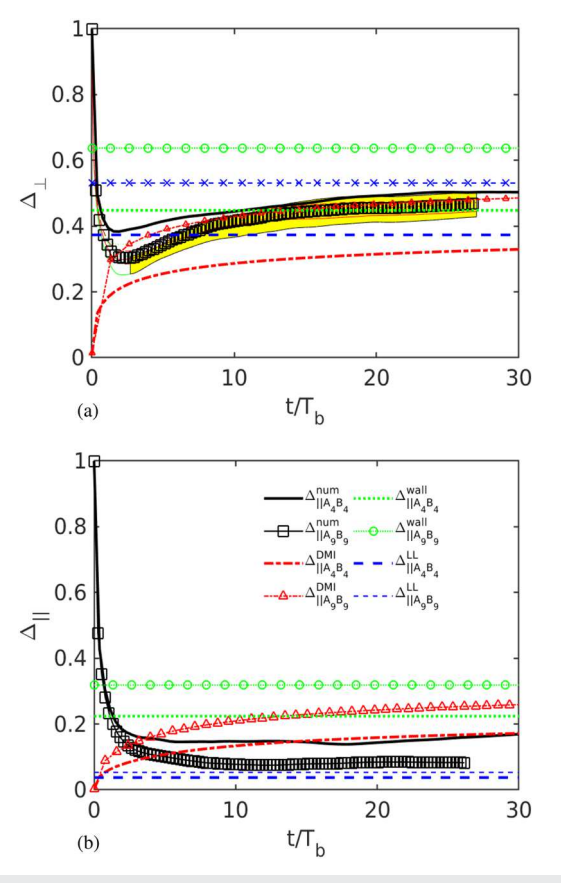


FIG. 15. Temporal evolution of Δ , the MSD excess as defined in Eqs. (22) and (23), obtained for micelle initial position X_0^n , (a) in the perpendicular direction and (b) in the parallel direction. The time is scaled by the bending time T_b , whose value is indicated in Table VI. Lines correspond to micelle A_4B_4 , and symbols correspond to A_9B_9 . The black and red colors refer, respectively, to the present work and the theoretical prediction of DMI^{S4} (including both strain and bending contributions). The constant curves correspond to particle Brownian motion near a non-deformable solid interface (green color) and a liquid–liquid interface (blue color). The yellow shaded area indicates scattering when the number of trajectories is varied between 15 and 40.

micelles A_4B_4 and A_9B_9 initially placed at X_0^n . Since the micelle is freely moving, its motion is expected to be diffusive as $t\to\infty$. In this work, the interpretation of the deviation of the micelle Brownian motion near the bilayer from the diffusive motion in the bulk is limited to a relatively short time scale, compared with the diffusive time scale (and also τ_r). The probability density functions in Fig. 10 suggest that micelles A_4B_4 and A_9B_9 remain relatively close to their initial positions during a simulation time of $\approx 0.1\tau_d$ and $0.05\tau_d$, respectively. Thus, in this time range, it is possible to compare the MSD excess with the theories, which are all developed at a constant distance x_0 between the particle and the interface.

The limits corresponding to a particle near a non-deformable interface [Eqs. (24) and (25)] and a particle near an elastic membrane [Eqs. (26)–(29)] are also displayed in Fig. 15. Let us discuss those limits before comparing them with the simulations. Due to membrane elasticity, $\Delta^{DMI} \rightarrow \Delta^{wall}$ at long time but since the ratio

between the area compressibility and the shear modulus is large (a feature of lipid bilayers), the convergence of Δ^{DMI} toward the wall limit is achieved beyond the current measurement time. The red curves calculated with C=100 tend toward the green asymptote after $O(10\tau_d)$ in the perpendicular direction and after $O(\tau_d)$ in the parallel direction (far beyond the maximum time in this figure). If the bilayer is supported by a solid wall, the Brownian motion of a nearby nanoparticle tends to Δ^{wall} quite quickly as shown by the experiments of Benavides-Parra. However, if the bilayer undergoes thermal undulation in the solvent and considering only the bilayer bending rigidity, Bickel has shown that Δ would theoretically converge to Δ^{LL} as $t\to\infty$ (the bilayer is indeed a fluid interface) if the separation distance between the particle and the bilayer is larger than the membrane correlation length (due to an external potential for instance).

Back to the simulation results, the MSD excess in the perpendicular direction is larger than that in the parallel direction, as expected. The temporal evolution of the MSD excess is similar for both micelles when the time is scaled by the bending time T_b . At $t \rightarrow 0$, Δ starts from 1 in the simulations, since the MSD is equal to 0 at the first instant. At short times, Δ decreases since the MSD varies such as a power law with a scaling exponent $\alpha > 1$. This is different from the DMI theory, where the starting point is the diffusive motion. Δ_{\perp} increases with time, starting from $t \approx T_b$, where the motion becomes subdiffusive. The MSD excess closely follows the DMI theory in the perpendicular direction (the yellow region shows the scattering when the number of trajectories is varied between 15 and 40 for the largest micelle). Thus, we conclude that bilayer bending rigidity plays a dominant role in terms of the modification of micelle mobility in that direction. However, in the parallel direction, the simulations and the DMI theory seem to tend toward different limits. This observation is particularly true for the largest micelle, since $\Delta_{\parallel} \rightarrow \Delta_{\parallel}^{LL}$, and most likely, it is associated with the negligible shear modulus of the lipid bilayer in the simulations. A substantial amount of computer resources is required in order to quantify the shift between the MSD excess of the smallest and largest micelles and to determine the role associated with the micelle finite size with respect to the bilayer characteristic length or with the soft nature of those nano-particles.

VI. CONCLUSION

Mesoscopic simulations were used to investigate the Brownian motion of a soft nanoparticle (micelle made from monomer assembly) of few tens of nanometers close to a soft interface (constituted of a lipid bilayer). The membrane's mechanical properties, particularly its bending rigidity, agree with the data available in the literature on DMPC lipid bilayers. After characterizing the particle diffusive motion in the bulk and the bilayer mechanical properties, the motion of the micelle was investigated for two positions near the bilayer and for two micelle sizes whose hydrodynamic diameters were around 2.5 and 5 times the membrane thickness, corresponding to ≈ 10 and 20 nm, respectively. Apart from the membrane length (set by the box size) and the estimated capillary length (associated with the very small but finite surface tension), the membrane has no other correlation length.

The particle trajectories were measured at different distances x_0 from the membrane, with a measurement time smaller than the

particle diffusion time scale so that the particle remains relatively close to its initial position. The numerical results obtained with two particle sizes suggest that (i) the micelle dynamics depends on the separation distance between the micelle and the membrane, (ii) the motion is subdiffusive only in the direction perpendicular to the membrane, and (iii) the MSD excess corresponding to the micelle Brownian motion tends to different limits in the parallel and perpendicular directions. The subdiffusive motion observed close to the membrane has some implications, for instance, in drug delivery applications. Preceding the endocytosis mechanism, the subdiffusive motion can lead to an increase in the intake time scale, or said differently, the number of successful attempts to approach the surface (that can be predicted in the frame of a Fokker–Planck approach, for instance) can be significantly lowered compared to the isotropic diffusive motion situation.²⁵

The results of this study were obtained in the particular situation where the particle diffusion time scale is comparable with (or larger than) the membrane relaxation time. They were carried out at time scales that are hardly accessible to experimental measurements (the diffusion time of a 10 nm particle is of the order of 0.1 μ s), and in that sense, they can provide valuable insights into the rapid dynamics of such small objects. In terms of the perspectives of the present work, a quantitative model that rationalizes the effect of micelle size and softness as well as the membrane mechanical properties requires a more significant amount of data from independent trajectories.

ACKNOWLEDGMENTS

This work was granted access to the HPC resources of IDRIS under the allocations 2022-[A0112A12031] and 2023-[A0132A12031] made by GENCI and to computational resources provided by the computing meso-center CALMIP under Project No. P1002. S.S., B.L., and M.A. acknowledge the financial support from the University of Toulouse and Région Occitanie via Grant No. ALDOCT-001118. A.M. and Z.L. acknowledge the financial support from the National Science Foundation via Grant Nos. OAC-2103967 and CDS & E-2204011.

AUTHOR DECLARATIONS

Conflict of Interest

The authors have no conflicts to disclose.

Author Contributions

S. Sheikh: Investigation (equal); Methodology (equal); Software (equal); Validation (equal); Visualization (equal); Writing – original draft (equal). B. Lonetti: Funding acquisition (equal); Investigation (equal); Supervision (equal); Writing – original draft (equal); Writing – review & editing (equal). I. Touche: Data curation (equal); Software (equal); Validation (equal). A. Mohammadi: Software (equal); Validation (equal). Z. Li: Investigation (equal); Methodology (equal); Software (equal); Supervision (equal); Writing – review & editing (equal). M. Abbas: Conceptualization (lead); Funding acquisition (lead); Investigation (equal); Methodology (equal);

Resources (lead); Supervision (lead); Validation (lead); Writing – original draft (lead); Writing – review & editing (lead).

DATA AVAILABILITY

The data that support the findings of this study are available from the corresponding author upon reasonable request.

REFERENCES

- ¹G. J. Doherty and H. T. McMahon, "Mechanisms of endocytosis," Annu. Rev. Biochem. **78**, 857–902 (2009).
- ²D. M. Richards and R. G. Endres, "The mechanism of phagocytosis: Two stages of engulfment," Biophys. J. **107**, 1542–1553 (2014).
- ³V. Francia, D. Montizaan, and A. Salvati, "Interactions at the cell membrane and pathways of internalization of nano-sized materials for nanomedicine," Beilstein J. Nanotechnol. 11, 338–353 (2020).
- ⁴Y. Lu and K. Park, "Polymeric micelles and alternative nanonized delivery vehicles for poorly soluble drugs," Int. J. Pharm. **453**, 198–214 (2013).
- ⁵J. Happel and H. Brenner, *Low Reynolds Number Hydrodynamics* (Kluwer, Dordrecht, 1991).
- ⁶M. D. Carbajal-Tinoco, R. Lopez-Fernandez, and J. L. Arauz-Lara, "Asymmetry in colloidal diffusion near a rigid wall," Phys. Rev. Lett. **99**, 138303 (2007).
- ⁷M. Lavaud, T. Salez, Y. Louyer, and Y. Amarouchene, "Stochastic inference of surface-induced effects using Brownian motion," Phys. Rev. Res. 3, L032011 (2021).
- ⁸H. Eral, J. Oh, D. Van Den Ende, F. Mugele, and M. H. G. Duits, "Anisotropic and hindered diffusion of colloidal particles in a closed cylinder," Langmuir **26**, 16722–16729 (2010).
- ⁹S. Villa, G. Boniello, A. Stocco, and M. Nobili, "Motion of micro- and nanoparticles interacting with a fluid interface," Adv. Colloid Interface Sci. **284**, 102262 (2020).
- ¹⁰S. Lee, R. Chadwick, and L. Leal, "Motion of a sphere in the presence of a plane interface. Part 1. An approximate solution by generalization of the method of Lorentz," J. Fluid Mech. 93, 705–726 (1979).
- ¹¹J. C. Benavides-Parra, D. Jacinto-Méndez, G. Brotons, and M. D. Carbajal-Tinoco, "Brownian motion near a liquid-gas interface," J. Chem. Phys. 145, 114902 (2016).
- ¹²S. Villa, C. Blanc, A. Daddi-Moussa-Ider, A. Stocco, and M. Nobili, "Microparticle Brownian motion near an air-water interface governed by direction-dependent boundary conditions," J. Colloid Interface Sci. 629, 917–927 (2023).
- ¹³T. Bickel, "Brownian motion near a liquid-like membrane," Eur. Phys. J. E 20, 379 (2006).
- ¹⁴ A. Daddi-Moussa-Ider and S. Gekle, "Brownian motion near an elastic cell membrane: A theoretical study," Eur. Phys. J. E 41, 19 (2018).
- ¹⁵F. Jünger, F. Kohler, A. Meinel, T. Meyer, R. Nitschke, B. Erhard, and A. Rohrbach, "Measuring local viscosities near plasma membranes of living cells with photonic force microscopy," Biophys. J. **109**, 869–882 (2015).
- ¹⁶P. J. Hoogerbrugge and J. M. V. A. Koelman, "Simulating microscopic hydrodynamic phenomena with dissipative particle dynamics," Europhys. Lett. **19**, 155–160 (1992).
- ¹⁷A. Eriksson, M. Nilsson Jacobi, J. Nyström, and K. Tunstrøm, "On the microscopic foundation of dissipative particle dynamics," Europhys. Lett. 86, 44001 (2009).
- ¹⁸R. D. Groot and P. B. Warren, "Dissipative particle dynamics: Bridging the gap between atomistic and mesoscopic simulation," J. Chem. Phys. **107**, 4423–4435 (1997).
- ¹⁹Z. Li, Y.-H. Tang, X. Li, and G. E. Karniadakis, "Mesoscale modeling of phase transition dynamics of thermoresponsive polymers," Chem. Commun. 51, 11038–11040 (2015).
- ²⁰R. Kubo, "The fluctuation-dissipation theorem," Rep. Prog. Phys. 29, 255–284 (1966).

- ²¹ X. Fan, N. Phan-Thien, S. Chen *et al.*, "Simulating flow of dna suspension using dissipative particle dynamics," Phys. Fluids **18**, 063102 (2006).
- ²²V. Symeonidis, G. E. Karniadakis, and B. Caswell, "Schmidt number effects in dissipative particle dynamics simulation of polymers," J. Chem. Phys. **125**, 000018 (2006).
- ²³P. Espanol and P. Warren, Europhys. Lett. **30**, 191 (1995).
- ²⁴R. Groot and K. Rabone, "Mesoscopic simulation of cell membrane damage, morphology change and rupture by nonionic surfactants," Biophys. J. 81, 725–736 (2001).
- ²⁵S. Burgess, Z. Wang, A. Vishnyakov, and A. V. Neimark, "Adhesion, intake, and release of nanoparticles by lipid bilayers," J. Colloid Interface Sci. **561**, 58–70 (2020).
- ²⁶ M. Kranenberg and B. Smit, "Phase behavior of model lipid bilayers," J. Phys. chem B. 109, 6553 (2005).
- ²⁷ Z. Li, Y.-H. Tang, H. Lei, B. Caswell, and G. E. Karniadakis, "Energy-conserving dissipative particle dynamics with temperature-dependent properties," J. Comput. Phys. 265, 113–127 (2014).
- ²⁸P. M. Pieczywek, W. Plaziński, and A. Zdunek, "Dissipative particle dynamics model of homogalacturonan based on molecular dynamics simulations," Sci. Rep. 10, 14691 (2020).
- ²⁹ X. Li, L. Gao, and W. Fang, "Dissipative particle dynamics simulations for phospholipid membranes based on a four-to-one coarse-grained mapping scheme," PLoS One 11, e0154568 (2016).
- ³⁰R. Goetz, G. Gompper, and R. Lipowsky, "Mobility and elasticity of self-assembled membranes," Phys. Rev. Lett. 82, 221–224 (1999).
- ³¹W. K. den Otter, "Area compressibility and buckling of amphiphilic bilayers in molecular dynamics simulations," J. Chem. Phys. **123**, 214906 (2005).
- ³²S. E. Feller and R. W. Pastor, "On simulating lipid bilayers with an applied surface tension: Periodic boundary conditions and undulations," Biophys. J. 71, 1350–1355 (1996).
- ³³J. Nagle and M. Wiener, "Structure of fully hydrated bilayer dispersions," Biochim. Biophys. Acta, Biomembr. 942, 1–10 (1988).
- ³⁴ H. I. Petrache, S. W. Dodd, and M. F. Brown, "Area per lipid and acyl length distributions in fluid phosphatidylcholines determined by ²H NMR spectroscopy," Biophys. J. **79**, 3172–3192 (2000).
- ³⁵W. Rawicz, K. Olbrich, T. McIntosh, D. Needham, and E. Evans, "Effect of chain length and unsaturation on elasticity of lipid bilayers," Biophys. J. **78**, 533–539 (2000).
- ³⁶L. Gao, J. Shillcock, and R. Lipowsky, "Improved dissipative particle dynamics simulations of lipid bilayers," J. Chem. Phys. **126**, 015101 (2007).
- ³⁷W. Helfrich, "Elastic properties of lipid bilayers: Theory and possible experiments," Z. Naturforsch., C 28, 693 (1973).
- ³⁸U. Seifert, "Configurations of fluid membranes and vesicles," Adv. Phys. **46**, 13–137 (1997).
- 39 S. Safran, "Statistical thermodynamics on surfaces and interfaces," in *Frontiers in Physics* (Westview Press, 2003).
- ⁴⁰D. Bochicchio and L. Monticelli, *The Membrane xBending Modulus in Experiments and Simulations: A Puzzling Picture* (Elsevier, 2016).
- ⁴¹J. Nagle, M. Jablin, S. Tristram-Nagle, and K. Akabori, "What are the true values of the bending modulus of simple lipid bilayers?," Chem. Phys. Lipids **185**, 3–10 (2015)
- ⁴²S. Tristram-Nagle, H. I. Petrache, and J. F. Nagle, "Structure and interactions of fully hydrated dioleoylphosphatidylcholine bilayers," <u>Biophys.</u> J. 75, 917 (1998).
- ⁴³ Z. Levine, R. Venable, M. Watson, M. Lerner, J. Shea, R. Pastor, and F. Brown, "Determination of biomembrane bending moduli in fully atomistic simulations," J. Am. Chem. Soc. **136**, 13582–13585 (2014).
- ⁴⁴E. Brandt, A. Braun, J. Sachs, J. Nagle, and O. Edholm, "Interpretation of fluctuation spectra in lipid bilayer simulations," Biophys. J. **100**, 2104–2111 (2011).
- ⁴⁵S. Shkulipa, W. den Otter, and W. Briels, "Surface viscosity, diffusion, and intermonolayer friction: Simulating sheared amphiphilic bilayers," Biophys. J. 89, 823–829 (2005).

- ⁴⁶J. Wohlert and O. Edholm, "Dynamics in atomistic simulations of phospholipid membranes: Nuclear magnetic resonance relaxation rates and lateral diffusion," J. Chem. Phys. 125, 204703 (2006).
- ⁴⁷R. Merkel, E. Sackmann, and E. Evans, "Molecular friction and epitactic coupling between monolayers in supported bilayers," J. Phys. **50**, 1535–1555 (1989).
- ⁴⁸E. Evans and A. Yeung, "Hidden dynamics in rapid changes of bilayer shape," Chem. Phys. Lipids 73, 39–56 (1994).
- ⁴⁹ U. Seifert and S. Langer, "Viscous modes of fluid bilayer membranes," <u>Europhys. Lett. 23</u>, 71 (1993).
- ⁵⁰S. Shkulipa, W. den Otter, and W. Briels, "Simulations of the dynamics of thermal undulations in lipid bilayers in the tensionless state and under stress," J. Chem. Phys. **125**, 234905 (2006).
- ⁵¹ M. Hömberg and M. Müller, "The role of inertia and coarse-graining on the transverse modes of lipid bilayers," Europhys. Lett. **97**, 68010 (2012).
- ⁵² M. Renner, L. Wang, S. Levi, L. Hennekinne, and A. Triller, "A simple and powerful analysis of lateral subdiffusion using single particle tracking," <u>Biophys. J.</u> 113, 2452–2463 (2017).

- ⁵³P. Schurtenberger and M. E. Newman, "Characterization of biological and environmental particles using static and dynamic light scattering," in *Revival: Environmental Particles* (CRC Press, 1993).
- ⁵⁴ A. Daddi-Moussa-Ider, A. Guckenberger, and S. Gekle, "Long-lived anomalous thermal diffusion induced by elastic cell membranes on nearby particles," Phys. Rev. E 93, 012612 (2016).
- ⁵⁵J. Smeulders, J. Mellema, and C. Blom, "Changing mechanical properties of lipid vesicle bilayers investigated by linear viscoelastic measurements," Phys. Rev. A 46, 7708 (1992).
- ⁵⁶K. de Haas, G. Ruiter, and J. Mellema, "Linear viscoelasticity in lipid bilayers of vesicles," Phys. Rev. E **52**, 1891 (1995).
- ⁵⁷T. Kato and T. Seimiya, "Study on intermicellar interactions and micelle size distribution in aqueous solutions of nonionic surfactants by measurements of mutual diffusion and self-diffusion coefficients," J. Phys. Chem. **90**, 3159–3167 (1986).
- ⁵⁸J. Benavides-Parra, Ph.D. thesis, Université du Maine and El Centro de Investigacion y de Estudios Avanzados del Insituto Politécnico National, Cinvestav, 2017.